



## Structure of the 001 talc surface as seen by atomic force microscopy: Comparison with X-ray and electron diffraction results

Eric Ferrage, Gregory Seine, Anne-Claire Gaillot, Sabine Petit, Philippe De Parseval, Alain Boudet, Bruno Lanson, Jocelyne Ferret, Francois Marti

### ► To cite this version:

Eric Ferrage, Gregory Seine, Anne-Claire Gaillot, Sabine Petit, Philippe De Parseval, et al.. Structure of the 001 talc surface as seen by atomic force microscopy: Comparison with X-ray and electron diffraction results. European Journal of Mineralogy, E Schweizerbart Science Publishers, 2006, 18, pp.483-491. <10.1127/0935-1221/2006/0018-0483>. <hal-00192281>

**HAL Id: hal-00192281**

**<https://hal.archives-ouvertes.fr/hal-00192281>**

Submitted on 27 Nov 2007

**HAL** is a multi-disciplinary open access archive for the deposit and dissemination of scientific research documents, whether they are published or not. The documents may come from teaching and research institutions in France or abroad, or from public or private research centers.

L'archive ouverte pluridisciplinaire **HAL**, est destinée au dépôt et à la diffusion de documents scientifiques de niveau recherche, publiés ou non, émanant des établissements d'enseignement et de recherche français ou étrangers, des laboratoires publics ou privés.

# **Structure of the {001} talc surface as seen by atomic force microscopy: Comparison with X-ray and electron diffraction results**

Eric Ferrage<sup>1,\*</sup>, Grégory Seine<sup>2</sup>, Anne-Claire Gaillot<sup>3</sup>, Sabine Petit<sup>4</sup>, Philippe de Parseval<sup>5</sup>,  
Alain Boudet<sup>2</sup>, Bruno Lanson<sup>6</sup>, Jocelyne Ferret<sup>7</sup>, François Martin<sup>8</sup>

(1) Department of Mineralogy, The Natural History Museum, Cromwell Road, London,  
SW7 5BD, UK

(2) Centre d'Elaboration des Matériaux et d'Etudes Structurales, CNRS, 29 rue Jeanne  
Marvig, 31055 Toulouse Cedex 4, France

(3) Department of Earth and Planetary Sciences, Johns Hopkins University, 34 and N.  
Charles streets, Baltimore MD 21218, USA

(4) Université de Poitiers, CNRS UMR 6532 'Hydr'A.S.A.', 40 avenue du Recteur Pineau,  
F-86022 Poitiers Cedex, France

(5) LMTG, CNRS UMR 5563, Observatoire Midi-Pyrénées, 14 Av. Edouard Belin, 31400  
Toulouse, France

(6) Environmental Geochemistry Group, LGIT – Maison des Géosciences, Joseph Fourier  
University – CNRS, BP53, F-38041 Grenoble cedex 9, France

(7) Talc de Luzenac S.A., BP 1162, F-31036 Toulouse Cedex, France

(8) LASEH, UMR 6532 HYDR'ASA, Université de Limoges, 123 Av. Albert Thomas, Bât.  
Les Dryades, 87000 Limoges, France

\* Author to whom correspondence should be addressed: e-mail : e.ferrage@nhm.ac.uk

## Abstract

In this study the surface structure of a centimetre sized crystal of talc from the Trimouns deposit (Ariège, France) was imaged by atomic force microscopy. The direct image shows detailed characteristics of clay tetrahedral surfaces. The unit-cell dimensions obtained using atomic force microscopy ( $a_{\text{or}} = 5.47 \pm 0.28$  and  $b_{\text{or}} = 9.48 \pm 0.28$  Å) are found to be slightly higher, with an increased uncertainty, than those obtained using X-ray diffraction ( $a_{\text{or}} = 5.288 \pm 0.007$  and  $b_{\text{or}} = 9.159 \pm 0.010$  Å) and selected-area electron diffraction ( $a_{\text{or}} = 5.32 \pm 0.03$  and  $b_{\text{or}} = 9.22 \pm 0.05$  Å). Talc has a quasi-ideal surface, clean of strong structural distortion as compared to most of other clay minerals and unlikely surface relaxation. The observation on the obtained image of apparent cell dimension enlargement is then more likely attributed to instrumental artefacts, also responsible for scattered values of unit-cell parameters rather than related to any surface structural features.

Key-words : talc, atomic-force microscopy, surface structure, X-ray diffraction, selected-area electron diffraction.

## 1. Introduction

Because of its beneficial properties to manufactured products, talc is widely used in paper coating, paint, ceramics, and polymer industries. In the automotive industry, talc is added to polymers to stabilize and harden automobile spare parts such as fenders, dashboards, steering wheels, etc. However, because different talc varieties can exhibit a wide range of physical and chemical properties it is necessary to optimize the use of these different types of talc for specific industrial applications. In particular, it is necessary to take into account the

surface structure of talc which, for example, may or may not allow the epitaxial growth of polymers (Ferrage *et al.*, 2002).

Over the last decade, the availability of atomic force microscopes (AFM) has provided new insights into mineral reactivity by providing images of crystal growth or dissolution at the micro-to-nanometer scale (Hillner *et al.*, 1992a and b; Kuwahara *et al.*, 1998, 2001; Bosbach *et al.*, 2000; Lindgren, 2000; Bickmore *et al.*, 2001; Brandt *et al.*, 2003; Tournassat *et al.*, 2003; Aldushin *et al.*, 2004; Yokoyama *et al.*, 2005). AFM has also allowed the direct visualization of the outer surfaces of minerals by imaging either groups of atoms at the molecular scale (Drake *et al.*, 1989; Weisenhorn *et al.*, 1990; Hartman *et al.*, 1990; Johnson *et al.*, 1991; Drake & Hellmann 1991; Wicks *et al.*, 1992, 1993, 1998; Vrdoljak *et al.*, 1994; Kuwahara, 1999, 2001) or individual atoms (Lindgreen *et al.*, 1991; Wicks *et al.*, 1992; Vrdoljak *et al.*, 1994; Sokolov *et al.*, 1997, 1999). Because of their perfect cleavage along the {001} plane, which produces extremely flat external surfaces, phyllosilicates are especially well-suited for an AFM study.

The structure of talc differs from that of mica, chlorite or lizardite which were previously imaged by AFM (Hartman *et al.*, 1990; Wicks *et al.*, 1992, 1993, 1998; Vrdoljak *et al.*, 1994; Kuwahara, 1999, 2001; Lindgreen *et al.*, 1991). Talc structure presents two similar external tetrahedral faces which is suitable for microscopic observations. In addition, the excess of octahedral charges is compensated for by deficiency in tetrahedral charges (Martin *et al.*, 1999), and the 2:1 sheet remains neutral, the interlayer of talc being thus devoid of cations. Finally, the weak substitution in talc layers induce moderate structural distortions such as tilts or tetrahedral rotations.

In this article we report the first atomic force microscope images of the surface of a talc sample composed of very well-stacked layers from the Trimouns deposit (Ariège, France). Images of the talc surface obtained from traditional AFM in repulsive mode are

compared with data in the literature and structural parameters of the bulk structure obtained from X-ray diffraction (XRD) and selected-area electron diffraction (SAED).

## 2. Background

### 2.1. Geological setting and sampling

Talc (2:1 layer silicate) has a composition close to that of the  $[\text{Mg}_3\text{Si}_4\text{O}_{10}(\text{OH})_2]$  end-member but with minor amounts of Fe, Al and F, and traces of Mn, Ti, Cr, Ni, Na and K (Heller-Kallai & Rozenson, 1981; Noack *et al.*, 1986; Abercrombie *et al.*, 1987; Aramu *et al.*, 1989; Coey *et al.*, 1991; de Parseval *et al.*, 1991, 1993; Martin *et al.*, 1996, 1999). The sample comes from the Trimouns talc and chlorite deposit, located in the French Pyrenees, ~100 km south of Toulouse, at an altitude of 1,700 m. The origin of talc is well-established and is the result of the hydrothermal alteration of wallrock in a zone of intense shearing between the Saint Barthélémy dome and the low-grade Paleozoic metamorphic cover (Fortuné *et al.*, 1980; Moine *et al.*, 1982, 1989; de Parseval *et al.*, 1993). Dolostones of the Paleozoic cover were transformed to talc, whereas the more siliceous and aluminous rocks (micaschists and granitic pegmatites) evolved to a chlorite-dominant ore characterized by well-defined metasomatic zones. The sampled talc of centimetric flakes that is commonly referred to as "talc flower" when mined, was formed within geodes in the dolomite hanging wall of the ore body and is associated with REE-minerals (de Parseval *et al.*, 1997).

### 2.2. Crystallographic data

Talc is a 2:1 phyllosilicate structure (Fig. 1a) with two Si tetrahedral sheets (forming an array of hexagonal rings of  $\text{SiO}_4$  tetrahedra – Fig. 1b) each linked through the apical

oxygen to either, and leading to the presence in between of a sheet of octahedrally coordinated  $Mg^{2+}$  cations. Early structural characterizations of talc have described its structure as monoclinic (*C-1* space group – Gruner, 1934), but later publications have described it as triclinic (*C-1* space group - Rayner & Brown, 1973) or as pseudomonoclinic (*Cc*) but using a *P-1* space group (Perdikatsis & Burzlaff, 1981). In comparison to aluminous phyllosilicates the misfit in lateral dimensions between tetrahedral and octahedral sheets is smaller, leading to a better accommodation of the two sheets. As a result, the tetrahedral rotation angle is diminished from  $\sim 13\text{-}14^\circ$  for muscovite to  $\sim 3\text{-}4^\circ$  for talc (Radoslovitch, 1961, 1962). The tetrahedral tilt angle out of the basal oxygen plane is very weak, giving an essentially flat  $\{001\}$  surface. The moderate tetrahedral rotations induce a reduction of the  $SiO_4$  ring symmetry from hexagonal into ditrigonal (Fig. 1b).

### 3. Experimental Methods

#### 3.1. Chemical analyses

The chemical composition of the talc sample used in this study was determined using a Cameca SX50 electron microprobe. The sample was included in a resin and polished to obtain perfect flat section. Operating conditions were 15 kV and 10 nA with beam size set to  $3 \times 3 \mu m$ . Standards used for calibration were: wollastonite for Si, corundum for Al, periclase for Mg, haematite for Fe, pyrophanite for Mn and topaze for F.

#### 3.2. X-ray diffraction

To obtain information on the crystallographic parameters, particularly in the *ab* plane, XRD data was collected on a randomly oriented sample. The centimetric talc flakes were ground to a fine powder in an agate mortar. XRD data was collected with a Bruker D5000

126 diffractometer equipped with a Kevex Si(Li) solid-state detector and CuK $\alpha$  radiation.  
127 Intensities were recorded at a 0.02°2 $\theta$  interval, from 2 to 90°, using a 50 sec counting time per  
128 step. Accuracy on 2 $\theta$  positions was better than 0.001°. A rotating sample holder was used to  
129 minimize the effect of preferential orientation. The openings of the divergence slit, the two  
130 Soller slits, the antiscatter slit, and the resolution slit were 0.5°, 2.3°, 2.3°, 0.5° and 0.06°,  
131 respectively. Cell parameters were refined using U-Fit 1.3 software assuming a *P-1* space  
132 group (Perdikatsis & Burzlaff, 1981).

### 134 3.3. <sup>57</sup>Fe Mössbauer spectroscopy

135 A <sup>57</sup>Fe Mössbauer absorption spectrum of the talc was collected over the range  $\pm 4$   
136 mm.s<sup>-1</sup> with a 512 channels analyzer. The Mössbauer spectrometer is composed of a compact  
137 detector  $\gamma$ -system for high-counting rates and of a conventional constant-acceleration  
138 Mössbauer device (WISSEL). A <sup>57</sup>Co (in Rh) source with nominal activity of 50 mCi was  
139 used. Talc flakes were finely ground under acetone (to minimize possible oxidation of Fe) and  
140 the resulting powder was placed in a plexiglas sample holder. The spectrum was recorded  
141 using a Canberra multichannel analyzer at 80°K to benefit from the second-order Doppler  
142 effect. The isomer shift was recorded with respect to  $\alpha$ -Fe metal. As recommended by  
143 Rancourt *et al.* (1992), the absorption thickness of the talc sample was calculated to minimize  
144 the width of the absorption lines using data from the phlogopite-annite series as phlogopite  
145 has a similar Fe-content to that of talc so as. The values are around 200 mg of mineral per  
146 cm<sup>2</sup>. Lorentzian lines shapes were assumed for decomposition, based on least-squares fitting  
147 procedures. The  $\chi^2$  and misfit values were used to estimate the goodness of fit.

### 149 3.4. Selected-area electron diffraction



The electron diffraction study was performed on a Philips 420 transmission electron microscope (TEM) equipped with a tungsten filament and operated at 120kV. Talc flakes were gently crushing in distilled water and dispersed onto a 3mm holey carbon-coated Cu-mesh TEM grid. Selected-area electron diffraction (SAED) patterns were recorded after orienting talc single crystals along the [001] zone axis using a double-tilt sample holder. The camera constant of the talc SAED patterns was calibrated using a gold reference sample with the crystals oriented along [100]. SAED patterns were recorded under the same parallel beam illumination conditions for both gold and talc samples. The error on the camera constant was estimated to be ~0.7%. Distances between diffraction spots were measured on the negatives using a precision measurement table.

### *3.5. Atomic force microscopy*

The talc surface was investigated by atomic force microscopy (AFM) using a Nanoscope II AFM from Digital Instruments. The talc sample was scanned in air using the repulsive contact mode with constant deflection. The D-head piezoelectric scanner was calibrated using HOP graphite and mica. The pyramidal shaped Si<sub>3</sub>N<sub>4</sub> cantilevers from Digital Instrument with 200 µm wide legs and a spring constant of 0.12 N.m<sup>-1</sup> were used. The talc sample was cleaved along {001} plane surface prior to observation using adhesive tape. Observations were performed using a vibration isolated platform and the thermal drift was minimized by waiting for the AFM to equilibrate with ambient temperature. Contact forces, scan speeds and scan directions were adjusted to optimize the resolution.

## **4. Results**

### *4.1. Mössbauer spectroscopy*

Table 1 lists the iron site-occupancies of the talc spectrum fitting, taking into account the quadrupole splitting distributions (Rancourt, 1994). The spectrum of the talc sample obtained at 80°K (Fig. 2a) is similar to talc spectra reported by Martin *et al.* (1999). It shows a difference in intensity between the two absorption bands, and a significant shoulder on the side of the -0.5 mm.s<sup>-1</sup> peak. A good fit to the experimental data was obtained with four Lorentzian doublets (Fig. 2b – Table 1). The first two, both with a large quadrupole splitting, are due to Fe<sup>2+</sup> in octahedral sites. The third doublet with a small quadrupole splitting and a low isomer shift is located within the first absorption band and attributed to Fe<sup>3+</sup> in the tetrahedral site (Dyar & Burns, 1986; Rancourt *et al.*, 1992; Rancourt, 1993; Martin *et al.*, 1999). The last doublet corresponds to Fe<sup>3+</sup> in octahedral sites (Blaauw *et al.*, 1980; Dyar & Burns, 1986; Rancourt *et al.*, 1992; Dyar, 1993; Rancourt, 1993; Martin *et al.*, 1999). According to this decomposition, Fe<sup>3+</sup> cations are thus present in both octahedral and tetrahedral sites. However, Fe<sup>2+</sup> is the dominant iron species (81%), thus indicating reducing conditions during the formation of talc.

#### 4.2. Chemical composition

The structural formula of the talc sample was calculated on the basis of eleven oxygens from the average of ten bulk analyses obtained by electron microprobe:

$$[\text{Mg}_{2.890}\text{Fe}^{2+}_{0.023}\text{Mn}^{2+}_{0.003}\text{Fe}^{3+}_{0.002}\text{Al}_{0.002}]_{\Sigma 2.917} [\text{Si}_{4.030}\text{Fe}^{3+}_{0.003}\text{Al}_{0.001}]_{\Sigma 4.034} \text{O}_{10} (\text{OH}_{1.975}\text{F}_{0.025})$$

The distribution of iron between <sup>[6]</sup>Fe<sup>2+</sup>, <sup>[4]</sup>Fe<sup>3+</sup> and <sup>[6]</sup>Fe<sup>3+</sup> was deduced from Mössbauer spectroscopy results. Aluminum was split into <sup>[4]</sup>Al and <sup>[6]</sup>Al to insure the neutralization of charges in the octahedral and the tetrahedral sheets, leading to the electroneutrality of the layer. The composition of the talc sample is thus very close to that of the representative talc determined by Martin *et al.* (1999) for the Trimouns deposit. Only minor substitutions are

present in the octahedral or tetrahedral sites leading to moderate local distortions in the tetrahedral sheet and thus to a nearly flat {001} surface.

#### 4.3. X-ray diffraction

The powder diffraction pattern of the ground talc powder is characteristic of pure talc with sharp 00 $\ell$  reflections that form a harmonic series ( $d_{001} = \ell \times d_{00\ell}$ ) thus indicating a well-ordered structure along the  $c^*$  axis without interstratification of chlorite layers (Fig. 3). Traces of quartz and dolomite are also detected. Sample unit-cell parameters were refined in the triclinic system ( $P-1$  space group - Perdikatsis & Burzlaff, 1981) from the positions of all measurable reflections between 2 and 90°2 $\theta$ . Unit-cell parameters from the present study are in agreement with those reported by Perdikatsis & Burzlaff (1981 – Table 2). It is possible to deduce the  $a_{or}$  and  $b_{or}$  dimensions of the usual C-centered pseudo-orthogonal unit cell from the refined abc unit-cell parameters defined in the triclinic system (Fig. 1b). As the  $\gamma$  angle is close to 120°,  $a_{or}$  is similar to  $a$  and  $b_{or}$  can be calculated as  $b_{or} = a_{or}\sqrt{3}$  (Table 2).

#### 4.4. Selected-area electron diffraction

The SAED pattern of a talc single crystal observed along the [001] zone axis contains very sharp  $hk0$  diffraction spots arranged according to a pseudo-hexagonal pattern (Figure 4). In order to determine unit-cell dimensions in the  $a^*b^*$  plane,  $a_1^*$ ,  $a_2^*$  and  $a_3^*$  distances were measured along [100], [010] and [110], respectively, and averaged to a single  $a^*$  dimension. Measurements were repeated for twelve crystals perfectly aligned along [001], and all values were then averaged to obtain a single  $a^*$  unit-cell dimension in the reciprocal space. However, in order to determine the unit-cell dimension in the  $ab$  plane in the direct space, it is necessary to take into account the 3D symmetry of the unit-cell:

$$a = (\sin \alpha / a^*) / [1 + 2 \cdot \cos \alpha \cdot \cos \beta \cdot \cos \gamma - \cos^2 \alpha - \cos^2 \beta - \cos^2 \gamma]^{-2} \quad (1)$$

As talc crystallizes in a triclinic system, unit-cell dimensions in the direct space cannot be simply deduced from the distances measured on the SAED pattern without making some assumptions for the values of  $\alpha$ ,  $\beta$  and  $\gamma$  angles. Therefore,  $\alpha$ ,  $\beta$  and  $\gamma$  values from XRD analysis (Table 2) were used in Eq. 1, and the following relationship was then obtained:

$$a = 1.1545/a^* \quad (2)$$

Note that the same relationship can be obtained, without using results from XRD, if one assumes that (i) the  $\gamma$  angle is close to  $120^\circ$ , and that (ii) the  $\alpha$  and  $\beta$  angles are between  $85^\circ$  and  $100^\circ$  then the approximations  $\sin\alpha \sim 1$  and  $\cos^2\alpha \sim \cos^2\beta \sim \cos\alpha \cdot \cos\beta \sim 0$  can be used. It follows that from direct measurements of the SAED patterns and from the relation given above (Eq. 2), it is possible to deduce that  $a_{\text{or}} = a = 5.32(3) \text{ \AA}$  and that  $b_{\text{or}} = a_{\text{or}} \sqrt{3} = 9.22(5) \text{ \AA}$  (Table 2).

#### 4.5. Atomic force microscopy

##### *Micro-topography of cleaved surface*

A high-resolution image was recorded to observe the talc surface micro-topography ( $500 \times 500 \text{ nm}^2$  – Fig. 5). Talc sample exhibits thick crystals in agreement with the macrocrystalline character of the investigated sample. A perpendicular section of talc topography is shown in Figure 5d and reveals that after cleavage these crystals are several tens of unit layers thick. This sample also has very large domains with flat surfaces which are particularly suitable for AFM imaging. Note the variation in Z direction on these almost flat regions that can be attributed to cantilever vibration which is greater when recording in air condition as contrast to images recorded in liquid (Kuwahara *et al.*, 1998, 2001). These regions were chosen for recording molecular-scale image.

## Molecular scale

The raw image obtained at the molecular scale ( $5 \times 5 \text{ nm}^2$  - Fig. 6) shows an alignment of triangles on the tetrahedral sheet surface. The of this raw image allows determining the  $m_i$  periodicity between adjacent triangles and the  $n_i$  periodicities for the second neighbor triangles along the perpendicular direction. Figure 7a shows the two-dimensional (2D) fast Fourier transform (FFT) of the raw image. On this numerical diffraction pattern, spots are distributed according to a pseudo-hexagonal pattern and different orders are visible that indicate a well-defined periodic surface structure. It is then possible to index these spots which correspond to  $m_i$  and  $n_i$  periodicities along two perpendicular directions in the raw image (Fig. 7b). The regularity of the structure deduced from the sharpness of the diffraction spots on 2D FFT is confirmed by direct periodicity measurements done on the raw image and reported in Figure 8, and leading to mean values of  $5.47 \pm 0.28 \text{ \AA}$  and  $9.48 \pm 0.28 \text{ \AA}$  for  $m_i$  and  $n_i$  periodic distances, respectively.

## 5. Discussion

### 5.1 Surface structure of talc

The raw image of talc surface (Fig. 6) is consistent with those found in the wealth of literature devoted to AFM studies of tetrahedral sheet surfaces of phyllosilicates. If some images present an arrangement of hexagonal rings corresponding to the basal oxygen plane of tetrahedral sheet other images, obtained on micas, show a bright spot periodicity of about  $5.1 - 5.3 \text{ \AA}$  (which could correspond to the layer unit-cell parameter of most phyllosilicates – Hartman et al., 1990; Lindgreen *et al.*, 1991; Wicks *et al.*, 1992, 1993; Vrdoljak *et al.*, 1994; Kuwahara, 1999, 2001). This periodicity was initially interpreted as the hexagonal array of interlayer cations but Kuwahara (1999) showed that it was possible to obtain both types of

image by varying the scan angle on the same sample. In addition, basal oxygen surface often show the alternation of high and low positions for any tetrahedron defining a hexagonal ring. This feature was first interpreted as resulting from the tetrahedral tilt of the basal oxygens but is now commonly considered as a topography artefact induced by the interaction between an asymmetric, double-atom, cantilever tip and the surface atoms (Gould *et al.*, 1989; Vrdoljak *et al.*, 1994; Wicks *et al.*, 1998; Kuwahara, 1999, 2001). According to these studies, triangles on the unfiltered image (Fig. 6) represent a height exaggerated of half of a tetrahedra. Thus, m- and n- periodicities between adjacent triangles correspond to  $a_{\text{or}}$  and  $b_{\text{or}}$  unit-cell dimensions of talc. Although the AFM image was recorded in air, the image is most likely of the basal oxygen surface rather than of some adsorbed species on the talc surface. Such adsorption would indeed result in a blurry image with holes and/or aggregation of these molecules. However, because cantilever drift easily removes interlayer cations from the mica surface, in spite of the strong electrostatic binding forces (Kuwahara, 1999, 2001), a similar “cleaning” of adsorbed species from the uncharged talc surface is most likely to occur.

The 2D FFT in which pseudo-hexagonal pattern was shown with different orders has indicated a well-defined periodic structure (Fig. 7). Back 2D FFT is commonly applied to remove extraneous signal from images but appears to be a controversial method. The two main criticisms are: i) important features of the raw image are removed and/or features that were not initially present are introduced, and ii) atomic positions are averaged. Wicks *et al.* (1998) discussed thoroughly these potential pitfalls, pointing out that the first point is essentially dependent on the competence of the user who should check carefully the FFT spots. Then, if all the structure information is used in the back 2D FFT operation, only high-frequency noise is removed, and the overall image enhancement does not affect structure details. Wicks *et al.* (1998) also demonstrated that following this image processing, atoms displaced from their ideal positions were not averaged as initially supposed. Figure 9a shows

the filtered image from the back 2D FFT of areas outlined on the numerical diffraction pattern (Fig. 7a). The filtered image (Fig. 9a) is essentially similar to the raw image (Fig. 6) but shows a spectacular enhancement of structural features, mainly alternate tetrahedra. The individual tetrahedra positions can be drawn to reveal the surface structure of talc (Fig. 9b). Note the presence of a small “hump” in the siloxane cavity. However, because of evident artefacts due in particular to the interaction between the double-atom cantilever tip and the sample, extreme care should be taken in the interpretation of these features in structural terms.

## 5.2 Talc unit-cell parameters

To determine the unit-cell dimension of the talc surface layer, approximately 100 measurements in each of the m and n three directions (corresponding to  $\mathbf{a}_{\text{or}}$  and  $\mathbf{b}_{\text{or}}$  directions, respectively) were performed on the raw images (Fig. 8). The frequency distribution of m and n indicates a single-mode distribution for each which agrees with published distributions (Vrdoljak *et al.*, 1994; Kuwahara, 1999, 2001).

The  $a_{\text{or}}$  and  $b_{\text{or}}$  parameters measured on the talc surface by AFM are  $5.47 \pm 0.28$  Å and  $9.48 \pm 0.28$  Å, respectively (Table 2). The uncertainty is quite high (~5% and 3% for  $a_{\text{or}}$  and  $b_{\text{or}}$ , respectively), but is consistent with other AFM studies on clay minerals (between ~2% and 8%, *e.g.*, Vrdoljak *et al.*, 1994; Kuwahara, 1999, 2001) regardless of the number of measurements performed on a single image and of the number of images processed. The obtained range for  $a_{\text{or}}$  and  $b_{\text{or}}$  parameters includes the values expected from the bulk structure determination although the mean values are high. Similar large unit cell parameters have been reported for other phyllosilicates, but the uncertainty systematically includes the ideal unit-cell dimensions (Vrdoljak *et al.* (1994) and Kuwahara (1999) on chlorite and muscovite, respectively). This enlargement of unit-cell parameters was attributed to surface relaxation. However, in contrast to micas or chlorite, no interlayer sheet or cation contributes to

interlayer cohesion in talc. As a result, surface relaxation is unlikely for talc and the observed variation in unit-cell dimensions may rather be attributed to instrumental effects as evoked by Vrdoljak *et al.* (1994). Note that improved unit-cell dimensions could be obtained by recording images in liquid environment rather than in air conditions as done in the present study (Kuwahara 1999, 2001; Sokolov *et al.*, 1997, 1999;).

Unit-cell dimensions obtained from XRD and SAED are consistent (Table 2) despite difficulties intrinsic to SAED such as the calibration of the camera constant, the alignment of a single crystal along [001] and the inability to precisely determine  $\alpha$ ,  $\beta$  and  $\gamma$  angles for a triclinic system. Moreover, the uncertainty on the measured values is low for the two methods ( $\sim 0.1\%$  and  $0.6\%$  for XRD and SAED, respectively – Table 2). In contrast,  $a_{\text{or}}$  and  $b_{\text{or}}$  parameters measured on the talc surface by AFM are scattered and the resulting uncertainty on the unit-cell parameter is much higher as discussed above. XRD and SAED (providing a good calibration of the camera constant) are more accurate methods to determine unit-cell parameters because of the improved statistics (for XRD) and of the enhanced sensitivity to crystal geometry.

Because the sample used in the present study presents a quasi-ideal surface structure with extremely limited tetrahedral tilts/rotations and limited, if any, surface relaxation, the variation in unit-cell dimensions can therefore rather be attributed to instrumental variability (calibration, tip-sample interaction). Extreme care should thus be used when interpreting the changes in unit-cell dimensions in terms of structural features for other clay minerals such as micas, kaolinities and chlorites in which such structural deformations are likely

## 6. Conclusion



In relation with the peculiar crystallinity of the studied talc sample from the Trimouns deposit (Ariège, France), it has been possible using atomic force microscopy to obtain a detailed image of the talc surface at the molecular scale. However, in spite of the high-quality image obtained, artefacts that lead to the observation of only one tetrahedron out of two were detected (double-atom cantilever tip interaction). In addition, the very peculiar crystal-chemistry of talc (very limited tetrahedral tilts and tetrahedral rotations, unlikely structure relaxation) has revealed the existence of additional instrumental effects. These effects lead to a slight distortion of the image that make a structural interpretation of these distortions, described in previous studies for other clay minerals (micas, chlorites), ambiguous. Finally the comparison of structure dimensions with data obtained by XRD and SAED shows AFM limitations for unit-cell dimensions determination because of the increased uncertainty and of the possible distortion (enlargement) by instrumental effects.

#### *Acknowledgements*

EF and FM are grateful to the S.A. Talc de Luzenac for financial support. TEM analyses were supported by NSF grant #EAR0409071. Fruitful discussions with Dirk Bosbach (INE – Karlsruhe, Germany) and instructive comments on an earlier version of the manuscript by Alain Baronnet (CRMCN Marseille, France) are also greatly acknowledged. This study has benefited of technical assistance from the Laboratoire de Chimie de Coordination (Toulouse, France) for Mössbauer analysis. The manuscript was much improved by the constructive reviews of Fred Wicks, Yoshihiro Kuwahara and AE Kenneth Livi.

## References

- Abercrombie, H.J., Skippen, G.B. and Marshall, D.D. (1987): F-OH substitution in natural tremolite, talc, and phlogopite. *Contrib. Mineral. Petr.*, **97**, 305-312.
- Aldushin, K., Jordan, G., Fechtelkord, M., Schmahl, W.W., Becker, H.W., Rammensee, W. (2004): On the mechanisms of apophyllite alteration in aqueous solutions. A combined AFM, XPS and MAS NMR study. *Clay. Clay Miner.*, **52**, 432-442.
- Aramu, F., Maxiav, G., Delunas, A. (1989): Mössbauer spectroscopy of talc minerals. *Nuovo Cimento*, **11D**, 891-896.
- Bickmore, B.R., Bosbach, D., Hochella, M.F., Charlet, L., Rufe E. (2001): In situ atomic force microscopy study of hectorite and nontronite dissolution: Implications for phyllosilicate edge surface structures and dissolution mechanisms. *Am. Mineral.*, **86**, 411-423.
- Blaauw, C., Stroink, G., Leiper, W. (1980): Mössbauer analysis of talc and chlorite. *J. Phys. I*, **41**, 411-412.
- Bosbach, D., Charlet, L., Bickmore, B.R., Hochella, M.F.J. (2000): The dissolution of hectorite: In-situ, real-time observations using Atomic Force Microscopy. *Am. Mineral.*, **85**, 1209-1216.
- Brandt, F., Bosbach, D., Krawczyk-Barsch, E., Arnold, T., Bernhard, G. (2003): Chlorite dissolution in the acid pH-range: A combined microscopic and macroscopic approach. *Geochim. Cosmochim. Ac.*, **67**, 1451-1461.
- Coey, J.M.D., Bakas, T., Guggenheim, S. (1991): Mössbauer spectra of minnesotaite and ferrous talc. *Am. Mineral.*, **76**, 1905-1909.
- De Parseval, P., Fontan, F., Aigouy, T. (1997): Composition chimique des minéraux de terres rares de Trimouns (Ariège, France). *C.R. Acad. Sci. II*, **234**, 625-630.

395 De Parseval, P., Fournes, L., Fortuné, J.P., Moine, B., Ferret, J. (1991): Distribution du fer  
 396 dans les chlorites par spectrométrie Mössbauer (57Fe) : Fe(III) dans les chlorites du  
 397 gisement de talc-chlorite de Trimouns (Pyrénées, France). *C.R. Acad. Sci. II*, **312**,  
 398 1321-1326.

399 De Parseval, P., Moine, B., Fortuné, J.P., Ferret, J. (1993): Fluid-mineral interactions at the  
 400 origin of the Trimouns talc and chlorite deposit (Pyrénées, France). in “Current  
 401 Research in Geology Applied to Ore Deposits”, P. Fenoll Hach-Ali, J. Torres-Ruiz, F.  
 402 Gervilla, eds. Univ. of Granada, Granada, 205-209.

403 Drake, B., Prater, C.B., Weisenhorn, A.L., Gould, S.A.C., Albrecht, T.R., Quate, C.F.,  
 404 Cannell, D.S., Hansma, H.G., and Hansma, P.K. (1989): Imaging crystals, polymers,  
 405 and process in water with atomic force microscope. *Science*, **243**, 1586-1589.

406 Drake, B. & Hellmann, R. (1991): Atomic force microscopy imaging of the albite (010)  
 407 surface. *Am. Mineral.*, **76**, 1773-1776.

408 Dyar, M.D. (1993): Mössbauer spectroscopy of tetrahedral Fe(III) in trioctahedral micas.  
 409 Discussion. *Am. Mineral.*, **78**, 665-668.

410 Dyar, M.D. & Burns, R.G. (1986): Mössbauer spectral study of ferruginous one-layer  
 411 trioctahedral micas. *Am. Mineral.*, **71**, 955-965.

412 Ferrage, E., Martin, F., Boudet, A., Petit, S., Fourty, G., Jouffret, F., Micoud, P., De Parseval,  
 413 P., Salvi, S., Saint-Gérard, Y., Buratto, S., Ferret, J., Fortuné, J.P. (2002): Talc as  
 414 nucleating agent of polypropylene : morphology induced by lamellar particles addition  
 415 and interface mineral-matrix modelisation. *J. Mater. Sci.*, **37**, 1561-1573.

416 Fortuné, J.P., Gavaille, B., Thiebaut, J. (1980): Le gisement de talc de Trimouns près de  
 417 Luzenac (Ariège). *Int. Geol. Congr.*, **26**, E10, 43 p.

418 Gould, S.A.C., Burke, K., Hansma, P.K. (1989): Simple theory for the atomic force  
 419 microscope with a comparison of theoretical and experimental images of graphite.  
 420 *Phys. Rev. B*, **40**, 5363-5366.

421 Gruner, J.W. (1934): The crystal structure of talc and pyrophyllite. *Z. Kristallogr. Krist.*, **88**,  
 422 412-419.

423 Hartman, H., Sposito, G., Yang, A., Manne, S., Gould, S.A.C., Hansma, P.K. (1990):  
 424 Molecular scale imaging of clay mineral surfaces with the atomic force microscope.  
 425 *Clay. Clay Miner.*, **38**, 337-342.

426 Heller-Kallai, L. & Rozenson, I. (1981): The use of Mössbauer spectroscopy of iron in clay  
 427 mineralogy. *Phys. Chem. Minerals*, **7**, 223-238.

428 Hillner, P.E., Gratz, A.J., Hansma, P.K. (1992a): Composite spiral growth kinetics of calcite  
 429 revealed by AFM. *P. Soc. Photo-Opt. Inst.*, **1639**, 160-170.

430 Hillner, P.E., Manne, S., Hansma, P.K. (1992b): Atomic-scale imaging of calcite growth and  
 431 dissolution in real time. *Geology*, **20**, 359-362.

432 Johnsson, P.A., Eggleston, C.M., Hotchella, M.F. Jr. (1991): Imaging molecular-scale  
 433 structure and microtopography of hematite with the atomic force microscope. *Am.*  
 434 *Mineral.*, **76**, 1442-1445.

435 Kuwahara, Y. (1999): Muscovite surface structure imaged by fluid contact mode AFM. *Phys.*  
 436 *Chem. Minerals*, **26**, 198-205.

437 Kuwahara, Y. (2001): Comparison of the surface structure of tetrahedral sheets of muscovite  
 438 and phlogopite by AFM. *Phys. Chem. Minerals*, **28**, 1-8.

439 Kuwahara, Y., Uehara, S., Aoki, Y. (1998) Surface microtopography of lath-shaped  
 440 hydrothermal illite by tapping-mode and contact-mode AFM. *Clay. Clay Miner.*, **46**,  
 441 574-582.

442 Kuwahara, Y. Uehara, S., Aoki, Y. (2001) Atomic force microscopy study of hydrothermal  
 443 illite in Izumiyama pottery stone from Arita, Saga Prefecture, Japan. *Clay. Clay*  
 444 *Miner.*, **49**, 300-309.

445 Lindgreen, H. (2000): Electrical conduction in layer silicates investigated by combined  
 446 scanning tunnelling microscopy and atomic force microscopy. *Clay Miner.*, **35**, 643-  
 447 652.

448 Lindgreen, H., Garnæs, J., Hansen, P.L., Besenbacher, F., Lægsgaard, E., Stensgaard, I.,  
 449 Gould, S.A., Hansma, P.K. (1991): Ultrafine particles of North Sea illite/smectite clay  
 450 minerals investigated by STM and AFM. *Am. Mineral.*, **76**, 1218-1222.

451 Martin, F., Ildefonse, P., Hazemann, J.L., Grauby, O., Decarreau, A. (1996): Random  
 452 distribution of Ge and Si in synthetic talc: an EXAFS and FTIR study. *Eur. J.*  
 453 *Mineral.*, **8**, 289-299.

454 Martin, F., Micoud, P., Delmotte, L., Marechal, C., Le Dred, R., De Parseval, P., Mari, A.,  
 455 Fortuné, J.P., Salvi, S., Beziat, D., Grauby, O., Ferret, J. (1999): The structural  
 456 formula of talc from the Trimouns deposit, Pyrénées, France. *Can. Mineral.*, **37**, 975-  
 457 984.

458 Moine, B., Fortuné, J.P., Moreau, P., Viguiier, F. (1989): Comparative mineralogy,  
 459 geochemistry and conditions of formation of two metasomatic talc and chlorite  
 460 deposits : Trimouns (Pyrénées, France) and Rabenwald (Eastern Alps, Austria). *Econ.*  
 461 *Geol.*, **84**, 1398-1416.

462 Moine, B., Gavaille, B., Thiebault, J. (1982): Géochimie des transformations à l'origine du  
 463 gisement de talc et chlorite de Trimouns (Luzenac, Ariège, France). I - Mobilité des  
 464 éléments et zonalités. *Bull. Mineral.*, **105**, 62-75.

465 Noack, Y., Decarreau, A., Manceau, A. (1986): Spectroscopic and oxygen isotopic evidence  
 466 for low and high temperature origin of talc. *Bull. Mineral.*, **109**, 253-263.

467 Perdikatsis, B. & Burzlaff, H. (1981): Strukturverfeinerung am Talk  $\text{Mg}_3\text{Si}_4\text{O}_{10}(\text{OH})_2$ . Z.  
 468 *Kristallogr.*, **156**, 177-186.  
 469 Radoslovitch, E.W. (1961): Surface symmetry and cell dimensions of layer lattice silicates.  
 470 *Nature*, **191**, 67-68.  
 471 Radoslovitch, E.W. (1962): The cell dimensions and symmetry of layer lattice silicates. I.  
 472 Some structural considerations. II. Regression relations. *Am. Mineral.*, **47**, 599-636.  
 473 Rancourt, D.G. (1993): Mössbauer spectroscopy of tetrahedral Fe(III) in trioctahedral micas.  
 474 Reply. *Am. Mineral.*, **78**, 669-671.  
 475 Rancourt, D.G. (1994): I. Inadequency of lorentzian-line doublets in fitting spectra arising  
 476 from quadrupole splitting distributions. *Am. Mineral.*, **21**, 244-249.  
 477 Rancourt, D.G., Dang, M.Z., Lalonde, A.E. (1992): Mössbauer spectroscopy of tetrahedral  
 478 Fe(III) in trioctahedral micas. *Am. Mineral.*, **77**, 34-43.  
 479 Rayner, J.H. & Brown, G. (1973): The crystal structure of talc. *Clay. Clay Miner.*, **21**, 103-  
 480 114.  
 481 Sokolov, I.Y., Henderson, G.S., Wicks, F.J. (1999): Theoretical and experimental evidence of  
 482 "true" atomic resolution under non-vacuum conditions. *J. Appl. Phys.*, **86**, 5537-  
 483 5540.  
 484 Sokolov, I.Y., Henderson, G.S., Wicks, F.J., Ozin, G.A. (1997): Improved atomic force  
 485 microscopy resolution using an electric double layer. *Appl. Phys. Lett.*, **70**, 844-846.  
 486 Tournassat, C., Neaman, A., Villiéras, F., Bosbach, D., Charlet L. (2003): Nanomorphology  
 487 of montmorillonite particles: Estimation of the clay edge sorption site density by low-  
 488 pressure gas adsorption and AFM observations. *Am. Mineral.*, **88**, 1989-1995.  
 489 Vrdoljak, G.A., Henderson, G.S., Fawcett, J.J., Wicks, F.J. (1994): Structural relaxation of the  
 490 chlorite surface imaged by the atomic force microscope. *Am. Mineral.*, **79**, 107-112.

491 Weisenhorn, A.L., Mac Dougell, J.E., Gould, Cox, S.A.C., Cox, S.D., Wise, W.S., Massie, J.,  
 492 Maivald, P., Elings, V.B., Stucky, G.D., Hansma, P.K. (1990): Imaging and  
 493 Manipulating Molecules on a Zeolite Surface with an Atomic Force Microscope.  
 494 *Science*, **247**, 1330-1333.

495 Wicks, F.J., Henderson, G.S., Hawthorne, F.C., Kjoller, K. (1998): Evidence for atomic-scale  
 496 resolution in atomic force microscopy of layer silicates. *Can. Mineral.*, **36**, 1607-1614.

497 Wicks, F.J., Kjoller, K., Eby, R.K., Hawthorne, F.C., Henderson, G.S., Vrdoljak, G.A. (1993)  
 498 Imaging the internal atomic structure of layer silicates using the atomic force  
 499 microscope. *Can. Mineral.*, **31**, 541-550.

500 Wicks, F.J., Kjoller, K., Henderson, G.S. (1992): Imaging the hydroxyl surface of lizardite at  
 501 atomic resolution with the atomic force microscope. *Can. Mineral.*, **30**, 83-91.

502 Yokoyama, S., Kuroda, M., Sato, T., (2005): Atomic force microscopy study of  
 503 montmorillonite dissolution under highly alkaline conditions. *Clay. Clay Miner.*, **53**,  
 504 147-154.

## Tables

**Table 1.** Mössbauer parameters of talc sample at 80 K. Quadrupole splitting ( $\Delta$ ) and isomer shift ( $\delta$ ) are given in  $\text{mm.s}^{-1}$ .

$\text{Fe}^{2+}$				$\text{Fe}^{3+}$				$\text{Fe}^{2+}$
$\delta^*$	$\Delta$	%	Site	$\delta^*$	$\Delta$	%	Site	$(\text{Fe}^{2+}+\text{Fe}^{3+})$
1.15	2.85			-0.25	0.21	12	[4]	
		81	[6]					81
1.21	2.96			0.07	0.68	7	[6]	

*Note:*  $\delta$  values relative to Fe-metal.

**Table 2.** Comparison of cell parameters. Distances are given in Angstroms and angles in degrees.  $a_{\text{or}}$  and  $b_{\text{or}}$  represent dimensions of the equivalent C-centered unit-cell with  $\gamma_{\text{or}} = 90^\circ$ .

	$a$	$b$	$c$	$\alpha$	$\beta$	$\gamma$	$a_{\text{or}}$	$b_{\text{or}}$
Perdikatsis & Burzlaff (1981)	5.291(3)	5.290(3)	9.460(5)	98.68(5)	85.27(5)	119.90(5)	5.293(4)	9.168(8)
XRD refinement (this study)	5.294(1)	5.281(1)	9.469(1)	98.71(1)	85.11(1)	119.98(1)	5.288(7)	9.159(10)
Electron diffraction (this study)	5.32(3)	-	-	-	-	-	5.32(3)	9.22(5)
AFM (this study)	-	-	-	-	-	-	5.47(28)	9.48(28)

*Note:* Unit-cell parameters from Perdikatsis & Burzlaff (1981) are transformed to appear in the  $C-I$  space group.



## Figure Captions

**Figure 1.** Talc structure along  $c^*$  (a) and the tetrahedral surface plane where a and b cell parameters in a quasi-orthogonal system ( $a_{or}$ ,  $b_{or}$ ) are indicated (b).

**Figure 2.** Experimental and fitted Mössbauer spectrum of talc sample at 80 K (a) and different components of the fitted spectrum (b).

**Figure 3.** X-ray-diffraction pattern of talc sample. Dol. and Qtz. represent dolomite and quartz traces, respectively.

**Figure 4.** SAED pattern of talc sample recorded along the [001] zone axis.

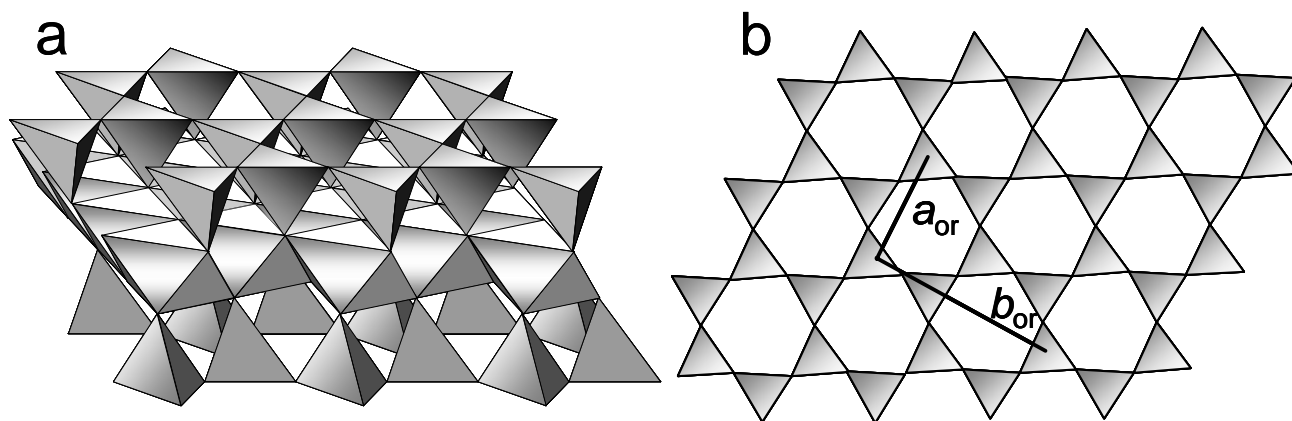
**Figure 5.** Micro-topography of talc surface (a) and the same image with isoaltitude curves separated by 70 Å to enhance topography contrasts (b). (c) and (d) represent profiles of cleaved surface morphology.

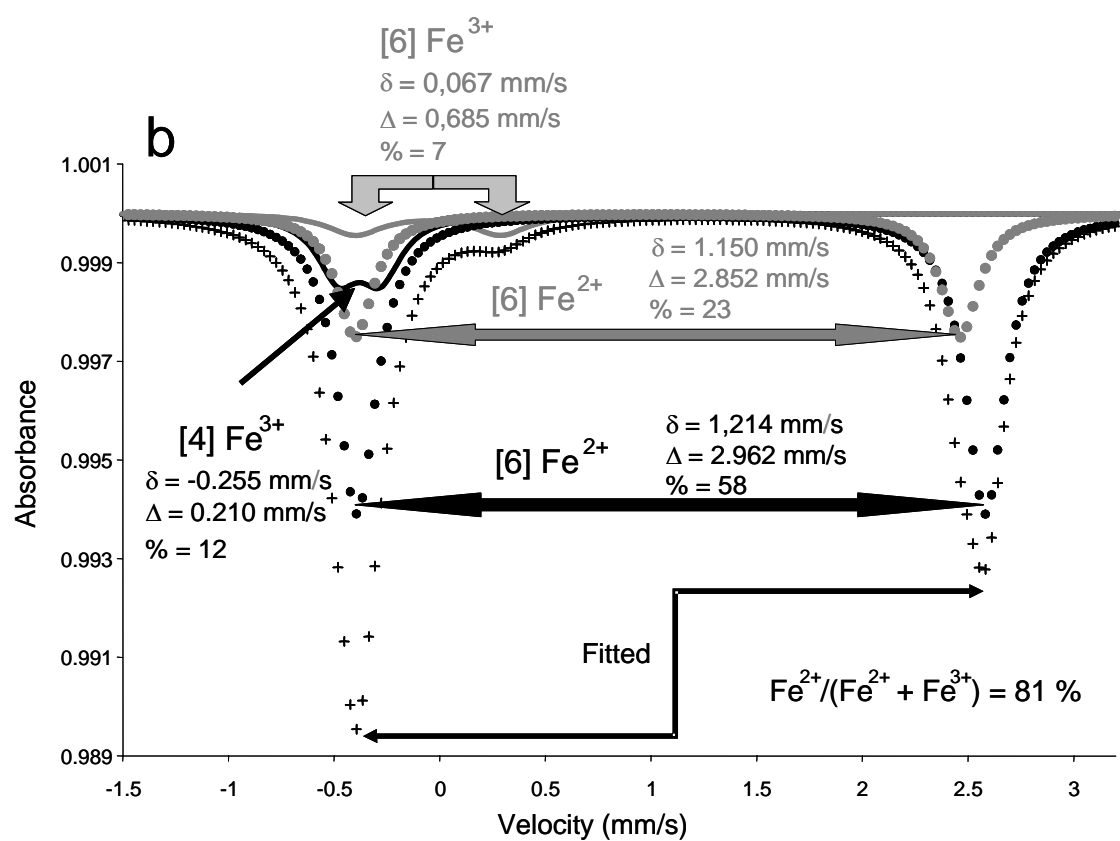
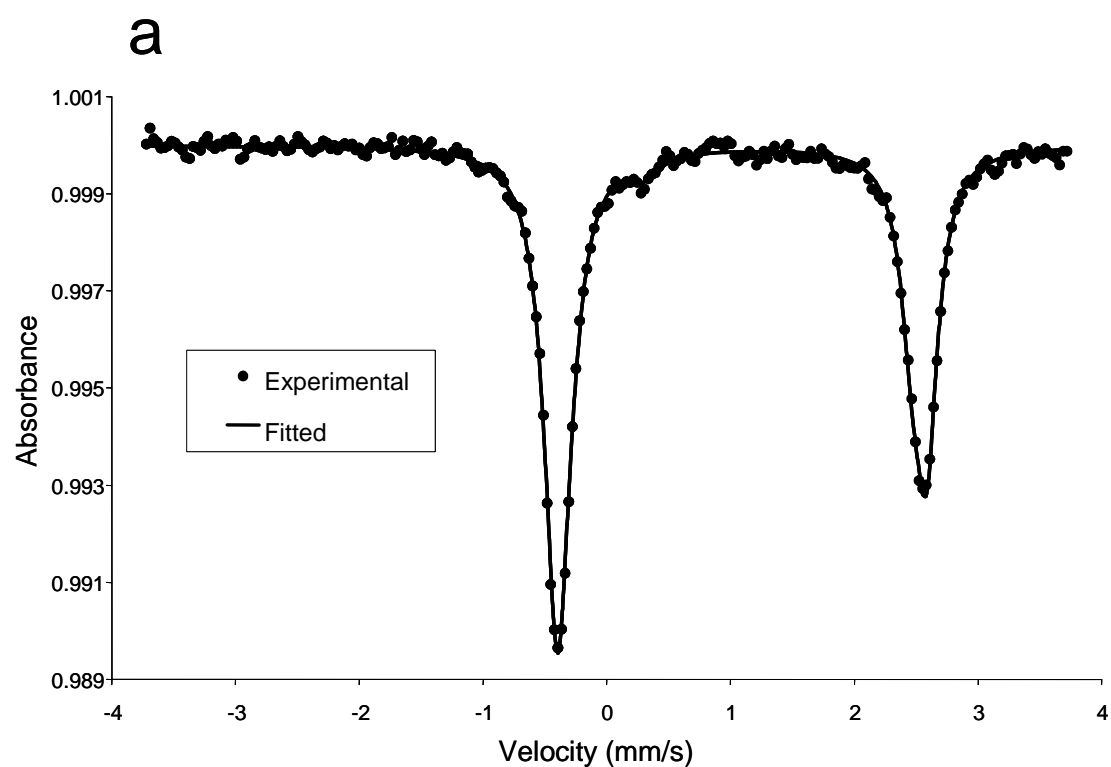
**Figure 6.** AFM image of talc surface at molecular scale  $5 \times 5 \text{ nm}^2$ .

**Figure 7.** Two-Dimensional Fourier Transform applied to molecular scale AFM image (Fig. 6 - a) and indexation of spots in reciprocal space (b).

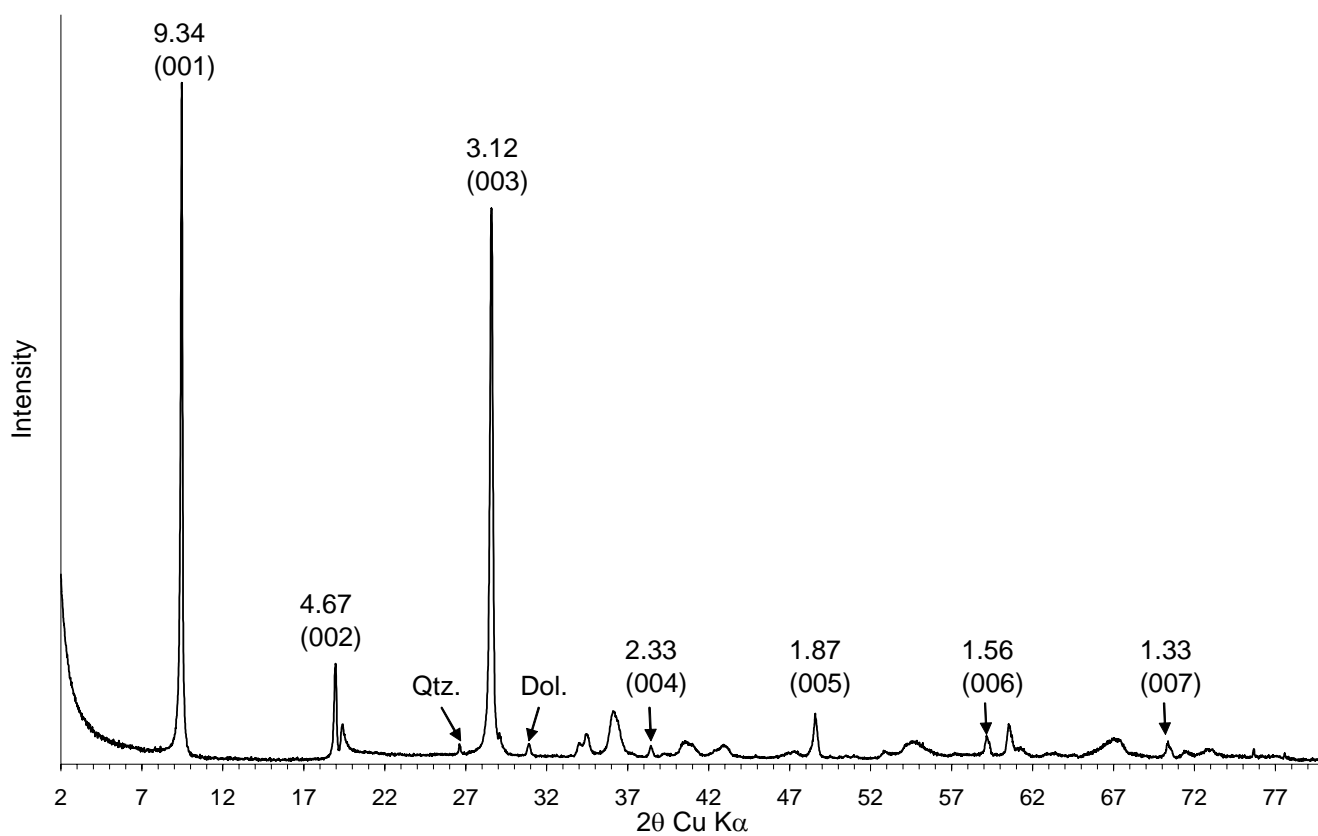
**Figure 8.** Histogram of  $a_{or}$  and  $b_{or}$  cell parameters from AFM molecular scale image.

**Figure 9.** Image shown in Fig. 5 after application of back 2D FFT to remove extraneous signal (a). An enlarged view of a image with a redraw of individual tetrahedrons (theoretical tetrahedral rotation not being taken into account).

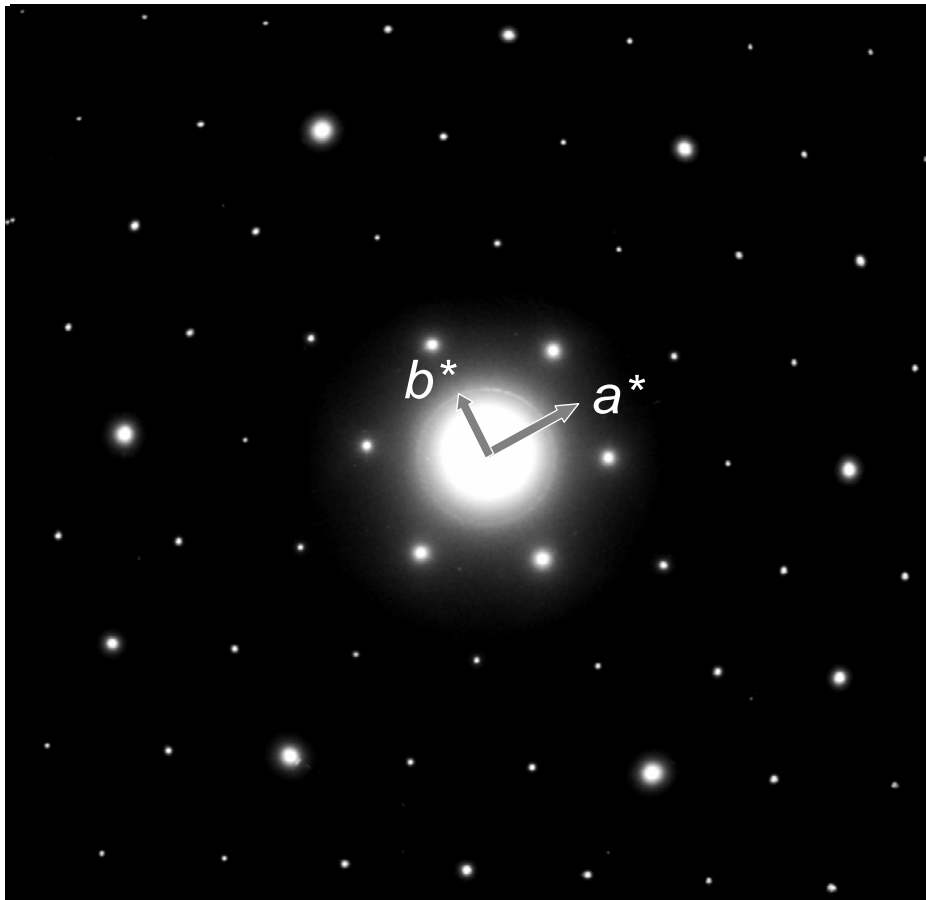




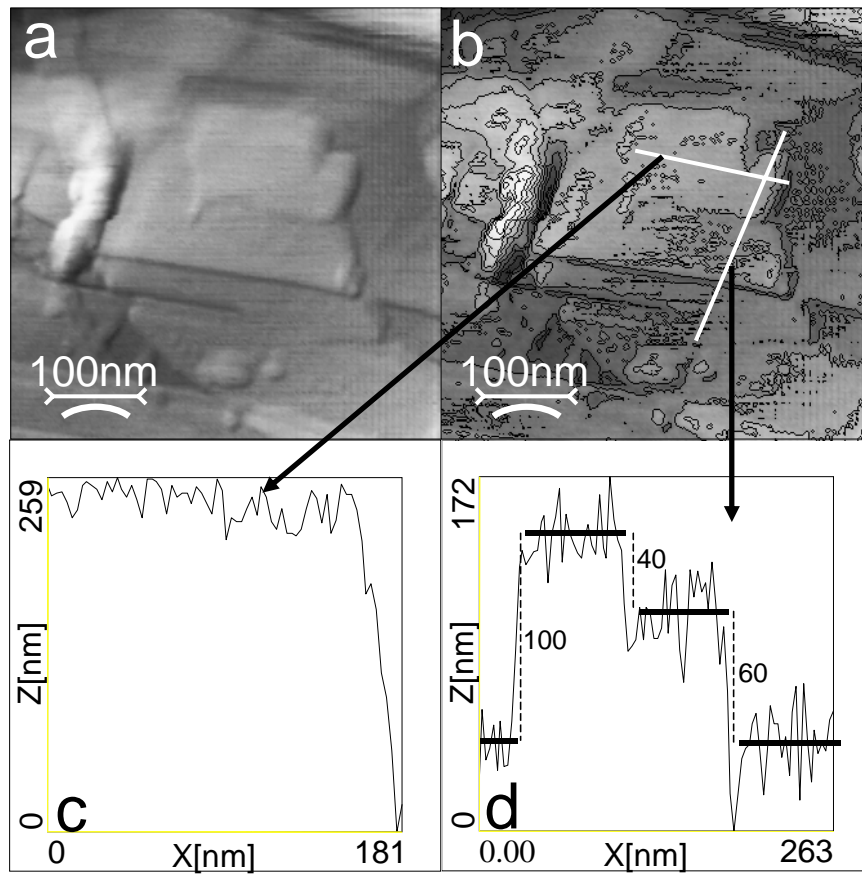
Ferrage et al., Fig. 02



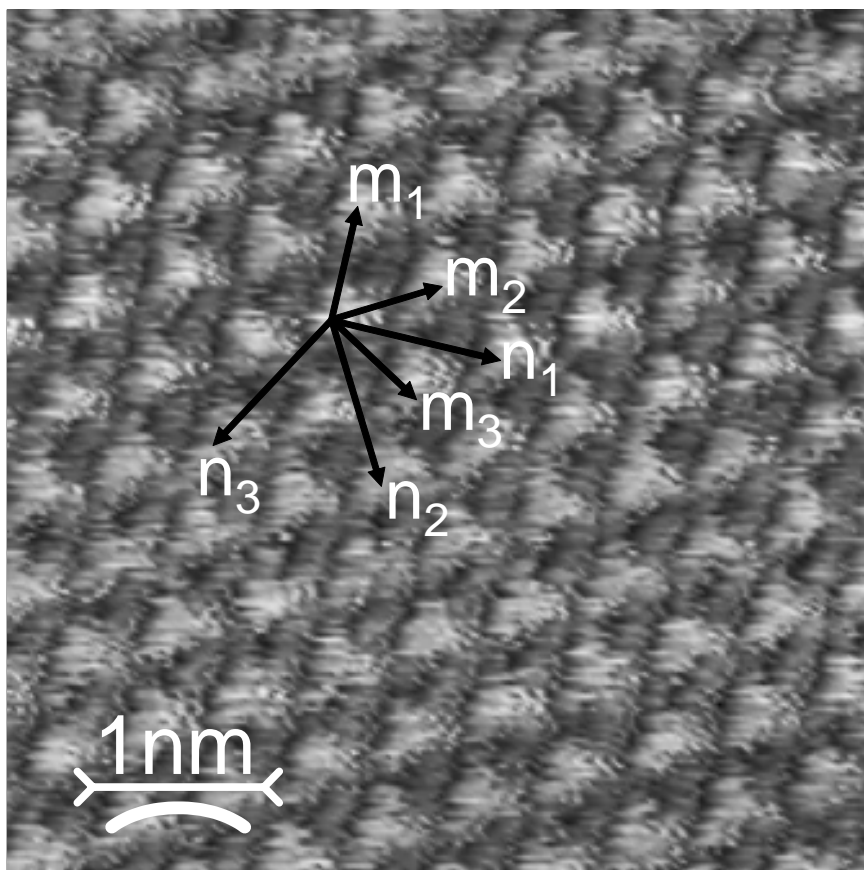
Ferrage et al., Fig. 03



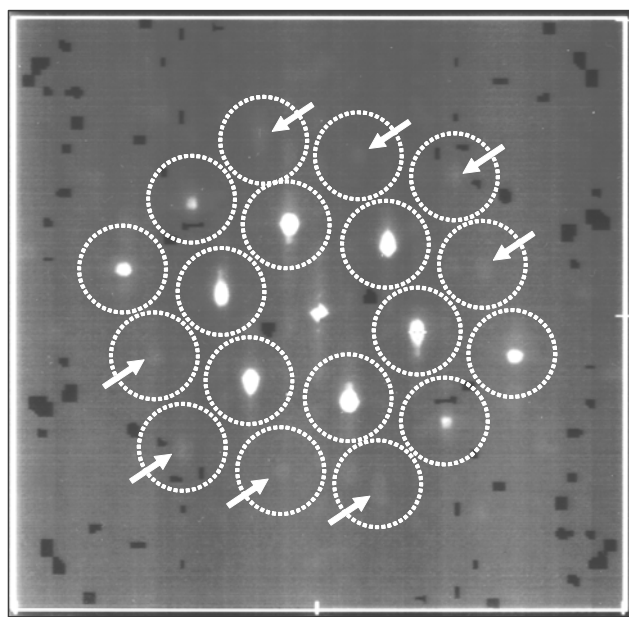
Ferrage et al., Fig. 04



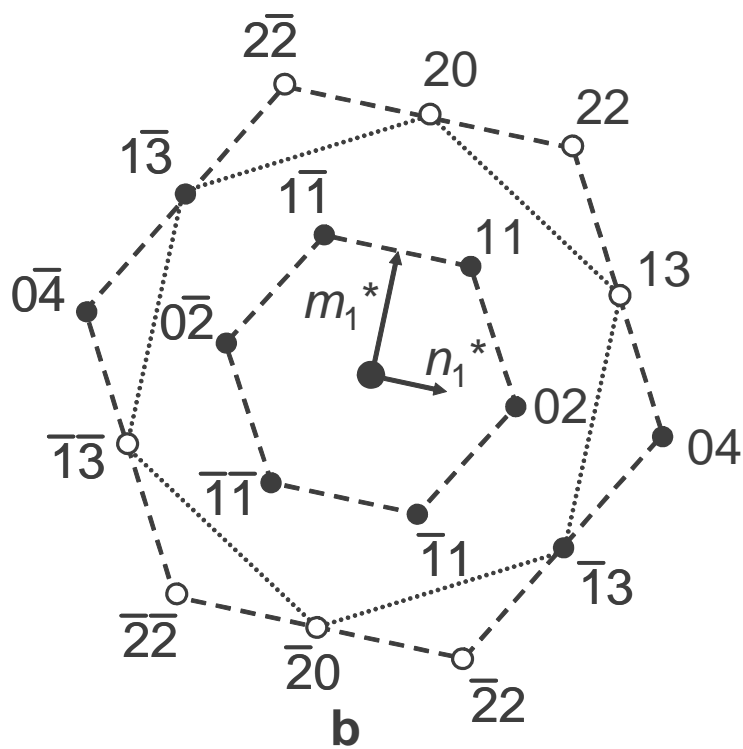
Ferrage et al., Fig. 05



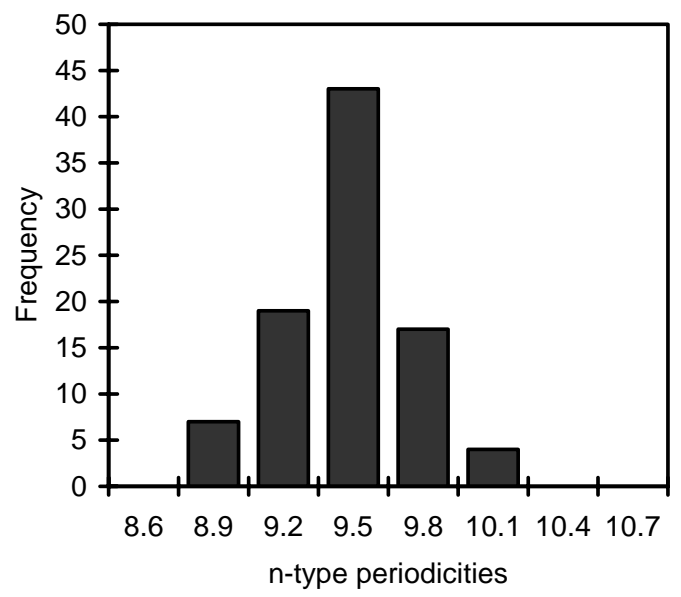
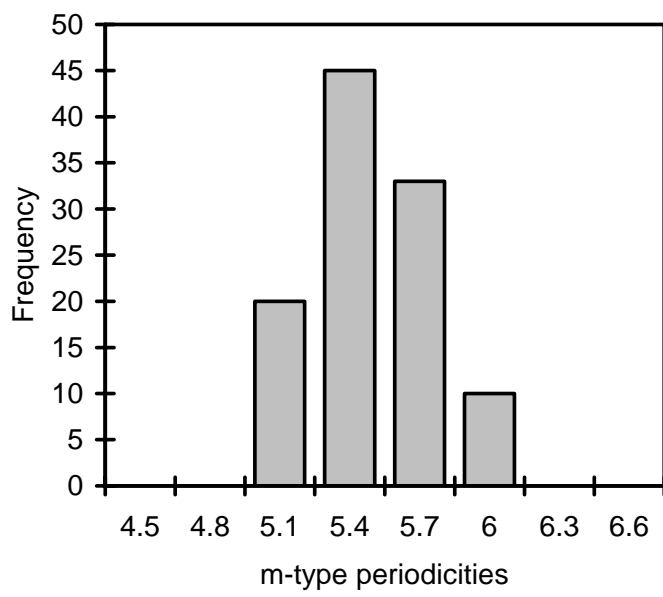
Ferrage et al., Fig. 06



a







Ferrage et al., Fig. 08

